Fig. 4. Impact of hyperthermia regimens on Th subset differentiation and Treg polarization. PBMC were stimulated with anti-CD3 mAb in the presence of PLGA scaffolds at different concentrations of GO (0.5, 1, 2 and 5%) in comparison to the control condition in red, second lane, at the two different hyperthermia regimens: NF (left panel) or t3 (right panel). **A)** Th1 (CD183+CD196−), Th1/Th17 (CD183+CD196+) and Th2 (CD183-CD196-CD194+), Th1/Th17 (CD183+CD196+) and Th17 (CD183-CD196+) phenotypes were evaluated. Furthermore, the expression of the T lymphocyte activation marker CD25 was assessed. **B)** Induction of Treg was evaluated by flow cytometry after six days and displayed as a percentage of CD45RA−FoxP3+CD25hi cells. Results are represented as violin plots showing median (thick line), 25th and 75th quartiles (*p < 0.05, **p < 0.01, ****p < 0.0001 versus control PBMC + antiCD3), N ≥ 3 individual experiments.

without reaching the complete suppression as observed with the NF protocol (Fig. 3B, right panel).

3.4. Effect of NIR radiation regimens in the differentiation of CD4⁺ T lymphocytes in different subsets

We investigated whether different hyperthermia protocols could impact CD4 lymphocyte differentiation in different Th subsets. Again, we observed that hyperthermia/irradiation does not affect the differentiation of both activated PBMCs and of activated PBMC cultured in presence of PLGA scaffolds, confirming the results previously reported for proliferation. Differences were instead observed after the application of the two hyperthermia regimens to activated PBMC in presence of PLGA-GO scaffolds. Again, we observed that NF irradiation strongly affects CD4⁺ lymphocyte differentiation. In fact, we noted that even 1% GO reduced differentiation toward the inflammatory Th1 subset. At increasing graphene concentrations, we detected a progressive impairment of T lymphocytes ability to differentiate toward Th1 subset
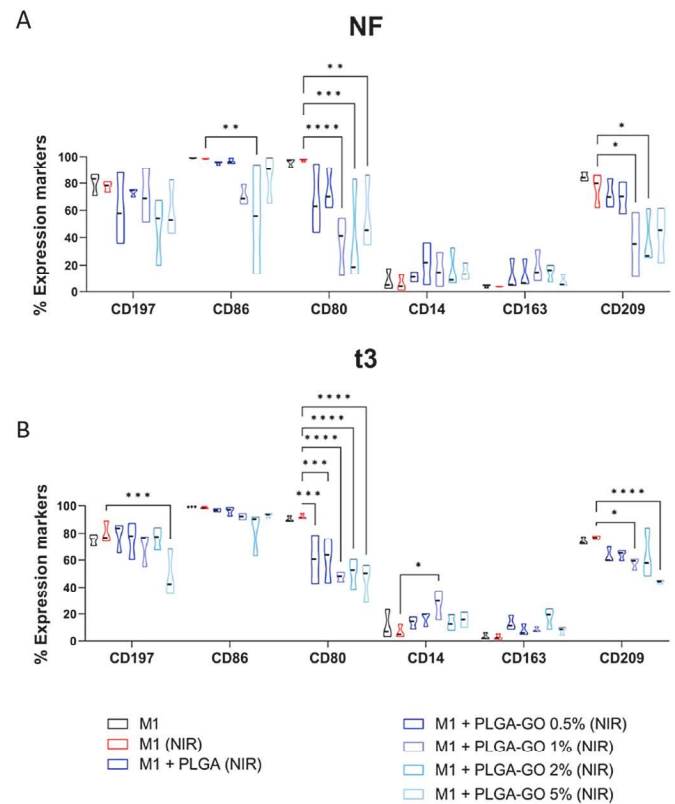

Fig. 5. Comparison of NF and t3 hyperthermia regimen on Monocyte to M1 macrophage differentiation. Phenotype analysis of PBMC differentiated into M1 macrophages in the presence of PLGA scaffolds at different concentration of GO (0.5, 1, 2 and 5%) in comparison to the control condition in red, second lane, represented by fully differentiated M1 macrophages treated with the same hyperthermia regimen, at the two different hyperthermia regimens: NF (**A**, upper panel) or t3 (**B**, lower panel). Scaffolds were added at the start of the differentiation protocol to evaluate the ability to affect monocyte differentiation toward M1 macrophages. At the end of the culture period, expression of CD14, CD209, CD197 and CD163 and of the co-stimulatory molecule CD80 and CD86 was evaluated by flow cytometry. Results are presented as a percentage of expression and are shown violin plots show median (thick line), 25th and 75th quartiles (*p < 0.05, ***p < 0.001, ****p < 0.0001 versus control M1), N ≥ 3 individual experiments.

(Fig. 4A, upper panel), which could be a consequence of reduced cell viability (Fig. 2).

A similar impairment in differentiation efficiency was observed also in the t3 protocol with 1% GO (Fig. 4A, lower panel). Both hyperthermia protocols did not significantly affect CD4 lymphocyte differentiation to Th2, while they significantly increased their polarization toward Th1/Th17 and Th17 in presence of PLGA-GO 2% scaffolds. Finally, we analyzed the expression of the T lymphocyte activation marker CD25. NF treatment heavily affected the expression of this marker similar to the effect previously observed for PBMC proliferation (Fig. 3A). In fact, 1% GO induced a strong reduction of CD25 expression, while the t3 protocol induced a slight reduction of CD25 expression (Fig. 4A).

Finally, we observed that both NF and t3 hyperthermia protocols reduced the polarization toward regulatory T cell subsets, but to a different extent. The NF regimen strongly decreased Treg polarization starting from 0.5% GO, while t3 protocol decreased Treg polarization when 2% GO was Other instead have shown that near-infrared (NIR) radiation, irrespective of its thermal effects, enhances the activation of both T helper (Th) 1 and Th2 immune responses, while it had no impact on regulatory T lymphocytes [42]. It is worth noting that these conflicting observations may arise from differences in experimental conditions, cell types, or specific parameters of photobiomodulation used in
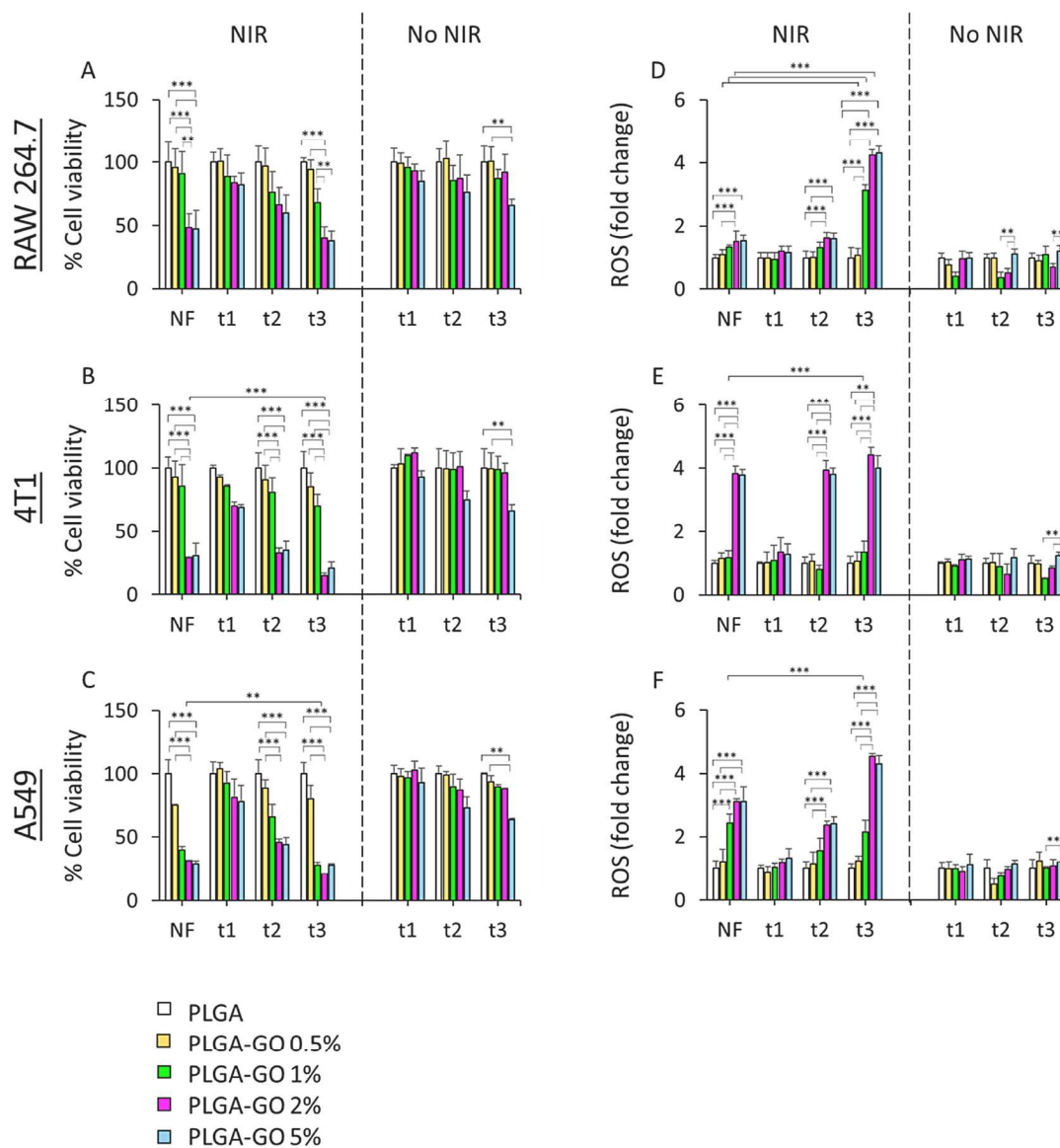
Fig. 6. Biological effect of photothermal/photodynamic treatments (NF and t3) on cells seeded on 3D printed PLGA-GO scaffolds. **A-C**) Cell viability on mouse macrophages, breast cancer cells and human lung adenocarcinoma cells respectively. **D-F**) Photodynamic-induced production of ROS after NF and t3 on mouse macrophages, murine breast cancer cells and human lung adenocarcinoma cells respectively. Results of cell viability are reported as % of cells seeded on LGA. Production of ROS are reported as fold change with respect to cells seeded on PLGA. **p > 0.01 and ***p > 0.001 ANOVA and Turkey post-hoc test.

the respective studies.

3.5. Comparison of NIR radiation regimens in the differentiation of monocyte toward M1 inflammatory macrophages

The differentiation process from monocyte to macrophage occurs, as indicated by the loss of expression of CD14, a monocytes marker, regardless of GO concentration and protocol used (Fig. 5A). On the other hand, however, both hyperthermia protocols significantly reduced the expression of the differentiation marker CD209 as well as the co-stimulatory molecule CD80 in presence of the higher GO concentrations (5, 2 and 1%) (Fig. 5A and B). These findings align with another study that demonstrated that high-intensity infrared photo-biomodulation (PBM) doses reduce markers associated with M1 and M2a macrophage phenotypes in vitro and increase the expression of TGFβ1 in M2 macrophages [43]. These results have also been corroborated by in vivo studies, which showed that PBM can reduce TNF-α expression in macrophages activated with LPS + IFN-γ.

3.6. Cell viability and ROS production

The two different NIR radiation protocols were then tested on different cell lines: A549 human lung adenocarcinoma cells, 4T1 mouse triple-negative mammary and RAW 264.7 mouse macrophage cell line.

Cells were cultured on PLGA-GO scaffolds to evaluate antitumor efficacy of the two distinct PTT/PDT regimens, NF and t3. NIR radiation was exerted on PLGA-GO scaffolds having GO at 0%, 0.5%, 1%, 2% and 5% w/w. In vitro evaluation of the two therapeutic strategies was first performed by comparing cell toxicity and production of ROS. Mouse macrophages seeded on PLGA-GO 2% and 5% scaffolds showed a significant decrease in cell viability after both NF and t3 with respect to irradiated PLGA and PLGA-GO 0.5%, while no significant differences were observed between the two therapeutic strategies in terms of viability (Fig. 6A). The two tested cancer cell lines depicted an evident decrease in cell viability after NIR radiation. Particularly, breast cancer cell lineage showed a significantly higher photothermal effect when seeded on PLGA-GO 2% and 5% scaffolds either on NF and on t3
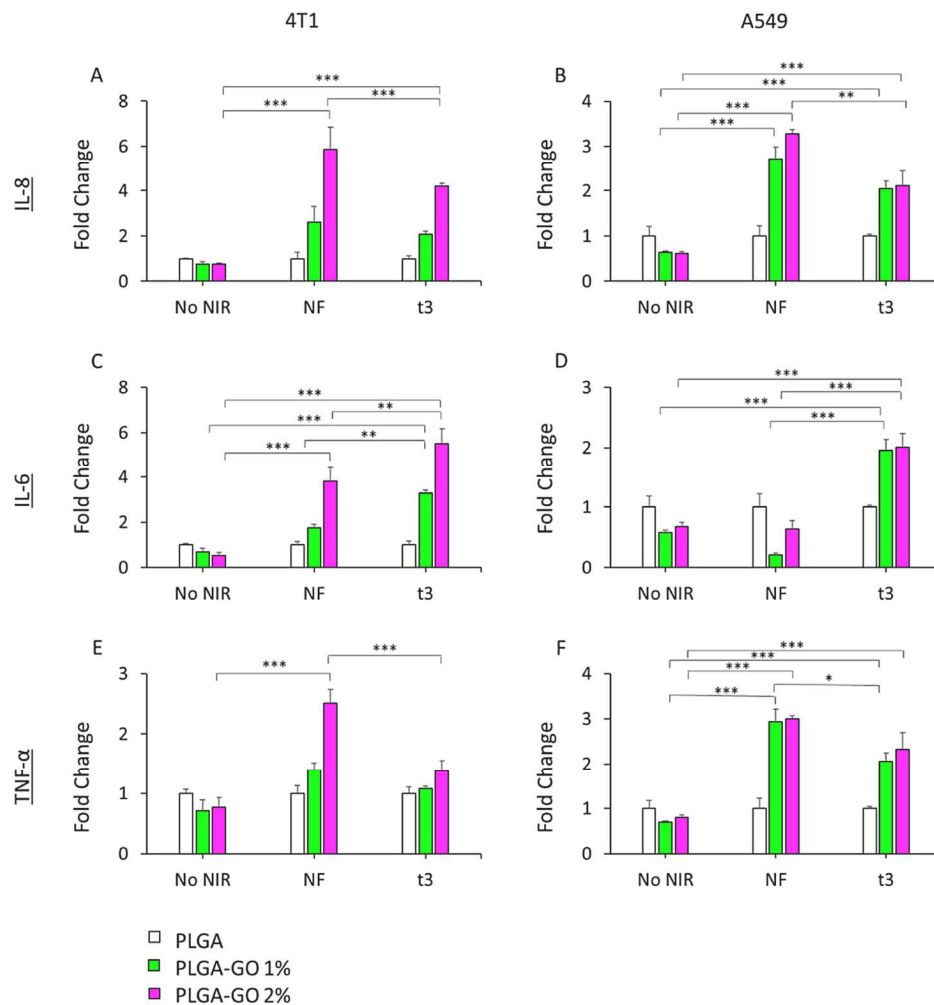
Fig. 7. Expression of cytokines on A459 and 4T1 cancer cell lines. **A, B**) Expression of IL-8 on mouse mammary tumor and on human lung adenocarcinoma respectively. **C, D**) Expression of IL-6 on mouse mammary tumor and on human lung adenocarcinoma respectively. **E, F**) Expression of TNF-α on mouse mammary tumor and on human lung adenocarcinoma respectively. Data are reported as fold change with respect to cells seeded on PLGA. **p > 0.01 and ***p > 0.001 ANOVA and Turkey post-hoc test.

(Fig. 6B). Importantly, t2 also caused a significant reduction in viability on the same samples with respect to irradiated PLGA and PLGA-GO 0.5%. Furthermore, we observed a slight difference between the two NIR therapies. The fractioned t3 radiation caused a significantly higher cell death on PLGA-GO 2% when compared to NF indeed, but not with PLGA-GO 5%. Human lung cancer cell lineage displayed a similar behavior (Fig. 6C). In this case, however, even cells seeded on PLGA-GO 1% had a strong reduction in cell viability after t3 and NF. The therapeutic strategy t3 showed a greater effect on PLGA-GO 1%, 2% and 5% samples with respect to NF. Importantly, for all tested cell lines, a significant reduction in cell viability was observed after seeding on PLGA-GO 5% without the need to perform NIR radiation, indicating an intrinsic toxicity effect probably due to the high concentration of GO. Taken together, these findings point out the different outcomes of two diverse therapeutic approaches based on NIR dose, showing a significantly greater effect on cancer cells after three radiations at the same temperature with respect to a single, longer NF administration. Moreover, the presence of GO in the scaffold holds potential for a specific PDT approach. When GO is exposed to NIR light, it undergoes a nonradiative relaxation process, transferring the absorbed energy to nearby oxygen molecules and generating singlet oxygen species through a type II photochemical pathway. The produced free radicals might exert potent cytotoxic effects by oxidizing biomolecules within the immediate vicinity of GO, leading to cellular damage and eventual cell death. This photodynamic effect of GO under NIR radiation holds immense potential for selective and precise cancer treatment, as it enables the generation of cytotoxic ROS exclusively within the targeted tumor regions while sparing the surrounding healthy tissues. For this reason, we investigated the production of ROS after the two different NIR radiation approaches. Mouse macrophages seeded on PLGA-GO 1%, 2% and 5% scaffolds showed a greater production of ROS when compared to NF therapy (Fig. 6D). Breast cancer cells showed a slightly higher production of ROS after NF, t2 and t3 only on samples seeded on PLGA-GO 2% and 5%. The effect at t3 was significantly greater than the one observed on NF for cells seeded on PLGA-GO 2%, but not on 5% (Fig. 6E). Human lung cancer cell lineage displayed a significantly higher ROS production on t3 with respect to NF, in accordance with murine breast cancer cells (Fig. 6F). However, in this case, even PLGA-GO 1% induced a strong production of ROS on cancer cells. For all samples, PLGA-GO 5% scaffolds caused a production of ROS even without NIR radiation, in accordance with the loss in viability, due to the high concentration of GO. Our experimental findings revealed that irradiated scaffolds containing 1% and 2% GO exhibited a remarkable increase in ROS production compared to the control scaffolds, resulting in a significant decrease in cancer cell viability. These observations suggest that the inclusion of GO at these concentrations enhances the oxidative stress on cancer cells, potentially leading to cell death. Conversely, scaffolds with 0.5% GO demonstrated cellular responses akin to those seen with PLGA

scaffolds alone, indicating that the presence of 0.5% GO did not significantly alter the cellular behavior compared to pure PLGA scaffolds. Scaffolds with 5% GO exhibited considerable toxicity even without NIR irradiation, particularly affecting non-cancerous cells, in accordance with findings on PBMC. The inherent toxicity observed at this GO concentration raised concerns about its potential adverse effects, moreover, the thermal effects induced by scaffolds containing 5% GO were found to be similar to those with 2% GO, suggesting that the higher GO concentration did not confer any additional advantage in terms of thermal properties. Considering these experimental results, we have excluded scaffolds with 0.5% (not effective) and 5% GO from further investigations.

These results highlight the crucial role of the presence of GO on inducing a cytotoxic effect mediated by the generation of free radicals. We observed that the concentration of GO in the 3D printed scaffolds represents a fundamental factor that must be taken into account due to the different biological effect observed on two cancer cell lines. Mouse breast cancer cells showed a higher sensitivity to scaffolds having 2% GO indeed, while lung cancer cells displayed a strong biological response even at 1% of GO. By tuning the right concentration of the photoabsorber, it is possible to achieve a selective destruction of tumor cells while minimizing damage to healthy tissues. Importantly, we observed that not only the concentration of GO, but also the selection of a proper NIR dose is crucial to modulate the production of ROS and cytotoxicity. The production of free radicals in mouse macrophages after t3 with respect to NF, along with its stronger killing effect on both tested cancer cell lineages can further enhance antitumor activity via activation and stimulation of the immune system towards cancer region, possibly inducing a long-lasting and specific immunogenic response [44, 45].

3.7. Effect of NIR radiation regimens on pro-inflammatory cytokines secretion by tumor cells

To investigate how NIR regimens could affect PLGA or PLGA-GO cultured tumor cells, pro-inflammatory cytokines release was assayed in cellular supernatants after treatments. NIR treatments were conducted on mouse 4T1 and human A549 cells as described above, and interleukin 8 (IL-8), tumor necrosis factor α (TNF-α) and interleukin 6 (IL-6) production was quantified in the culture supernatants by ELISA method (Fig. 7), as picograms of cytokines produced per cellular viability. IL-8 is a chemokine involved in the innate immune responses and in the recruitment of acute inflammatory cells, such as neutrophils and other granulocytes, and TNF-α and IL-6 are secreted under cellular oxidative stress condition. We demonstrated that the presence of GO in both percentages could affect the cellular secretion of proinflammatory elements under single and repeated NIR regimens. In our human cellular model, we observed a higher content of IL-8 and TNF-α upon both NIR regimens, as compared to not irradiated groups. Furthermore, cells revealed the same capability of cytokines production when cultured on PLGA-GO 1% and 2%, highlighting the responsiveness of the scaffold. The highest level of IL-6 secretion was found to be in t3 regimen. On the other hand, NIR treatment appeared to be more efficacious on cytokines production when 4T1 cells were cultured on PLGA-GO 2%, indicating a GO-dependent effect, taking also into account the cellular viability/mortality. TNF-α seemed to be less influenced when t3 regimen was applied.

3.8. Impact of NIR radiation regimens on immune response of mouse macrophages

The RAW264.7 cells are monocyte/macrophage-like cell lineage [46, 47] well-characterized with respect to macrophage-mediated immune, metabolic, and phagocytic functions [48]. To evaluate the performance of the PTT treatment on immune response, Raw 264.7 cells was cultured in the presence of PLGA and PLGA-GO scaffolds with or without NIR
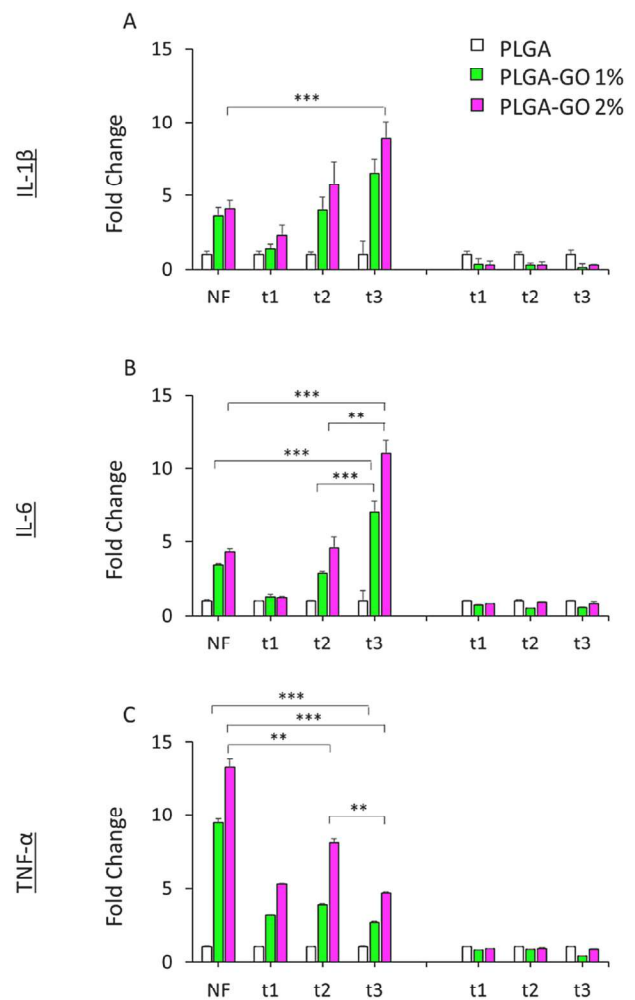

Fig. 8. Immune response of mouse macrophages. **A)** Expression of IL-1β by RAW264.7 cell line. **B)** Expression of IL-6 by RAW264.7 cell line. **C)** Expression of TNF-α by RAW264.7 cell line. Data are reported as fold change with respect to cells seeded on PLGA. ******p > 0.01 and *******p > 0.001 ANOVA and Turkey post-hoc test.

laser treatment and inflammatory cytokines secretion was investigated. Fig. 8 shows the production of IL-1β, IL-6 and TNF-α 24 h s after repeated and single NIR irradiation regimens. Inflammatory cytokines secretion by mouse Raw264.7 cells was observed to be both scaffold composition-dependent and time-dependent after NIR laser treatment. A significant time-dependent effect of NIR laser treatment on cytokines secretion was observed in the presence of PLGA-GO scaffolds. A very significant increase of TNF-α by RAW-264.7 macrophages was particularly observed 24 h s after single NIR treatment in the presence of PLGA-GO 2% scaffolds compared to the same samples irradiated with repeated NIR laser irradiation. A gradual increase of TNF-α was actually observed in the RAW-264.7 cells irradiated with repeated NIR treatment (48 h s after the second treatment). Then, a significant decrease of TNF-α and concomitant increase of IL-6 were observed 72 h s after RAW-264.7 cells irradiation (t3) in the presence of PLGA/GO 2% scaffolds [49]. We observed a significant increase of IL-6 in the culture medium of RAW-264.7 macrophages treated with single NIR irradiation, that was comparable to the value measured 24 h s after RAW-264.7 cells were exposed to 3-min NIR laser (t1 time point). IL-1β secretion increased in a NIR laser dose-dependent manner following repeated laser treatment. The single dose of NIR laser irradiation (NF) triggered an effective release of IL-1β in the culture medium by RAW-264.7 macrophages in comparison with the same cells exposed to 3 min-NIR laser irradiation,
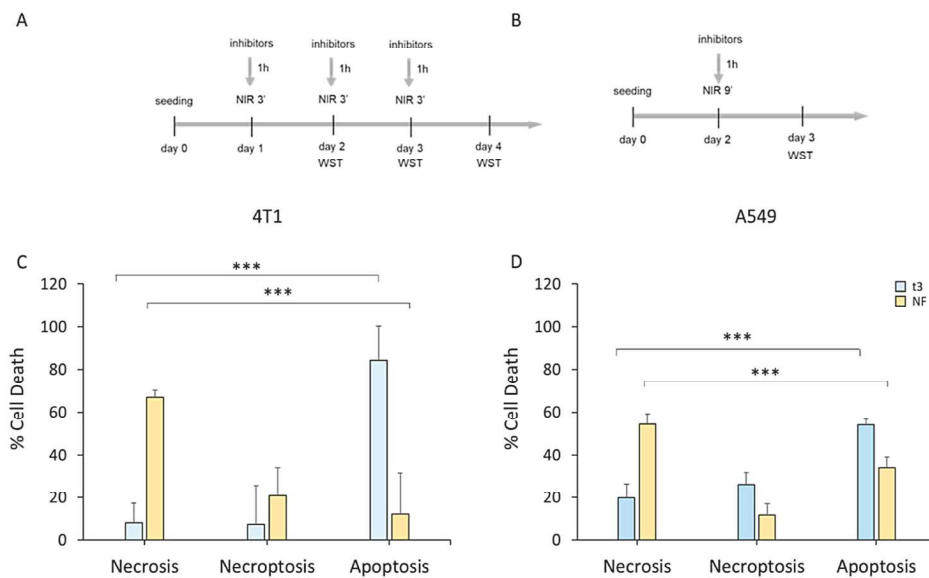
Fig. 9. Cell death induced on cancer cells after NIR treatment regimens. **A)** Schematic representation of the design of the experiments for apoptosis and necroptosis in the t3 NIR regimen. Caspase- or RIPK1-inhibitors were added three times into the wells at final concentrations of 20 μM before each NIR irradiation. **B)** Schematic representation of the design of the experiments for apoptosis and necroptosis in the NF NIR regimen. Caspase- or RIPK1-inhibitors were added once into the wells at final concentrations of 20 μM before NIR irradiation. **C)** Percentage of different types of cell death induced by NIR on mouse mammary tumor. **D)** Percentage of different types of cell death induced by NIR on mouse mammary tumor. ***p < 0.001 ANOVA and Turkey post-hoc test.

that released undetectable amounts of this cytokine, as measured 24 h s after laser treatment. The amount of IL-1β release, however, was smaller when compared to IL-1β amounts secreted by RAW-264.7 cells ater 72 h s post-repeated NIR laser irradiation.

3.9. Cell death pattern induced by photodynamic effects of PLGA-GO in cancer cells

PDT mediated hyperthermia can kill cells through induction of necrosis, apoptosis or through necroptosis [50,51]. We investigated whether different hyperthermia regimens could impact cell death pathway induced by means of NIR-activated PLGA-GO 2% scaffolds in cancer cell lines, we set up an in vitro assay treating first cells with specific cell death pathways inhibitors and then applying NIR laser irradiation at above indicated conditions [52]. We seeded 4T1 murine mammary carcinoma and human A549 lung carcinoma cells on PLGA-GO scaffolds in the presence of 20 μM pan-caspase inhibitor Z-VAD-FMK that blocks the induction of apoptosis or 20 μM 7-Cl-O-- Nec-1 (RIP1 inhibitor II) that selectively blocks RIP1-dependent necroptosis (Fig. 9A–B) [53–55]. After NF and t3 NIR irradiation, cell viabilities were then measured using WST-1 assay and different type of cell death were discriminated by the specific pathways inhibitor. Percentage of necrotic, necroptotic and apoptotic cells after repeated and single NIR irradiation regimens are showed in Fig. 9. Repeated 3-min NIR treatment killed 4T1 mouse breast cancer cells mainly through RIP-1-independent apoptosis (84,1%), while the cell death pattern switched to necrosis-dominant when the single 9-min NIR regimen was applied. Apoptosis was the principal cell death pathway (54%) also for A549 lung cancer cells treated with repeated 3-min NIR irradiations, even though necroptosis (26%) and necrosis (19,87%) play a role in the PLGA-GO2%-induced cell death. In contrast, single 9-min irradiation resulted in 54% of necrosis in A549 cells; notably this treatment also led to a mixed cell death pattern, considering apoptosis and necroptosis percentages (34 % and 11.9 %, respectively). These data demonstrate that cell death pathways executed upon NIR irradiation in cancer cells grown on GO-based scaffolds seem to be NIR laser dose-dependent. PDT killed tumor cells mainly through apoptosis when the NIR radiation was administered in three separate days (t3). Necrosis was, conversely, the

principal mechanism for PDT-induced cell death in the NF treatment regimen. A minor contribution of dose-induced necroptosis to cell death was observed in both cancer cell lines after photothermal/photodynamic treatment even though the difference between the percentages of this cell death mechanism was not statistically significant.

3.10. In vivo photo dynamic therapy

Since the in vitro experiments have demonstrated the high tumor selectivity and excellent antitumor property of scaffolds, their efficacy was investigated in vivo. Mice were inoculated subcutaneously with 4T1-Luc2 cells, expressing luciferase through lentiviral vector encoding firefly luciferase gene (luc2) under control of EF-1 alpha promoter. One week post tumor challenge, four groups were randomly established (n = 4): tumor (without adding any scaffolds or NIR (T), tumor and scaffold (TS), tumor, scaffold and a single NIR radiation of 9 min (NF), tumor, scaffold and 3 NIR radiations of 3 min each -one per day (t3). TS, NF and t3 groups went on subcutaneous surgical insertion of the PLGA-GO 2% scaffold beneath the tumor area. The 2% GO concentration was chosen in accordance with our in vitro findings on 4T1 cell lineage. After surgical insertion of the scaffolds, NIR radiation was carried out on mice keeping the power density fixed at 0.8 W/cm^2 as for the in vitro experiments. The two NIR radiation doses tested in vitro were administered also on tumor-bearing mice for PTT/PDT. To provide direct evidence of the photothermal/photodynamic properties of our scaffold in vivo, during NIR irradiation, thermographic images were captured using a thermal camera. A sharp rapid increase of the local tumor temperature after NIR irradiation was found when scaffolds were irradiated with NF or t3 doses while the tissue surrounding the tumor showed very little photothermal effects, reducing hyperthermia damage to the healthy tissue. T and TS groups did not show any potential temperature effects during the observation periods. (Fig. 10A). The local temperature of TS group was only around 35 °C, which is identical to the tumor temperature of T group. We evaluated the bioluminescence after intraperitoneal injection of D-luciferin using the Optical Imaging IVIS® System, by acquiring images every 7 days to monitor tumor growth. Results are shown in Fig. 10 in terms of luminescence intensity of the
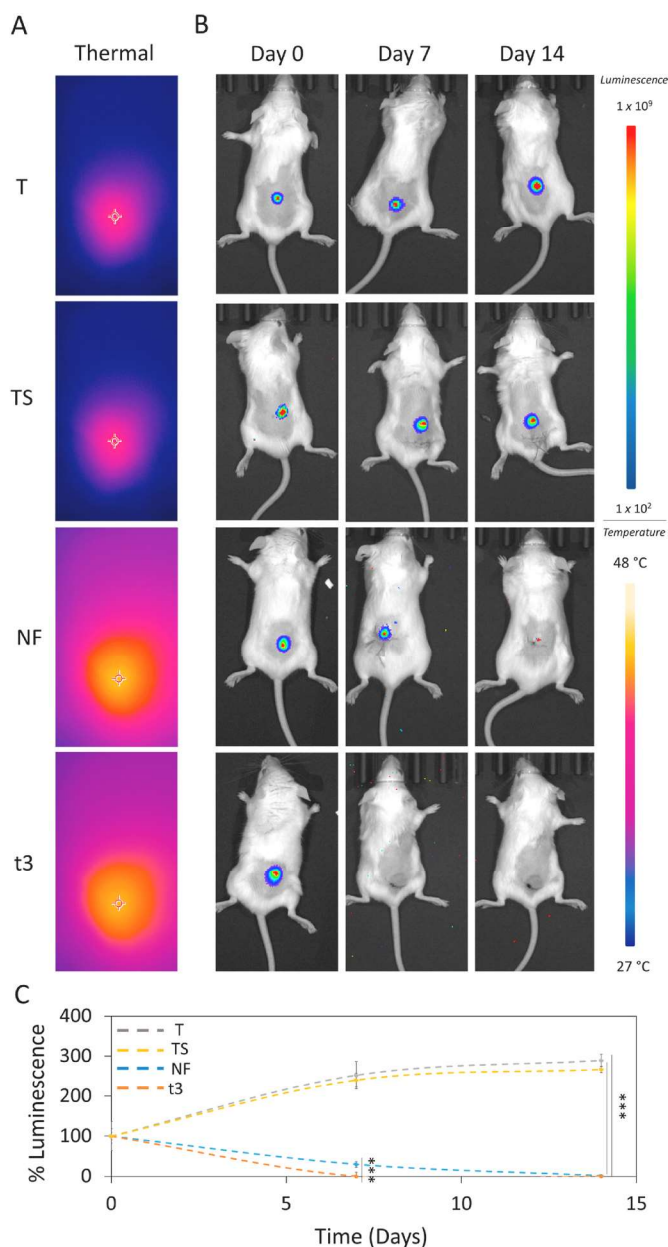
Fig. 10. In vivo NIR radiation. **A)** Images of the localized thermal increase with a thermal camera focused on cancer region in vivo. **B)** In vivo luminescence intensity on the four experimental groups (T, TS, NF and t3). **C)** Luminescence intensity over time. Luminescence was expressed as % of day 0 for each experimental group. ***p < 0.001 ANOVA and Turkey post-hoc test.

oxidized luciferin. After photothermal/photodynamic treatment, tumor bioluminescence in NF and t3 groups was observed to be remarkably reduced over time, where increased in T and TS groups. At the end of the 14th day no luminescence signal was observed in whole-body bioluminescent images of NF and T3 groups. However, a difference between the two therapeutic approaches was observed at day 7, as shown in the representative images of mice through IVIS® System (Fig. 10B). Mice treated with t3 showed strong reduction in bioluminescent tumor signal compared to the NF group. Luminescence intensity of luciferin was quantified and reported in Fig. 10C. Results are expressed as % luminescence intensity at 0, 7 and 14 days with respect to day 0 for each experimental group. After 7 days, NF group showed luminescence intensity reduced to 30%, with respect to its day 0, indicating a strong inhibition effect on tumor growth. Importantly, just after 7 days, we

observed no luminescence signal in all mice from t3 group, indicating that this tuning of the NIR dose administration exhibited the best effect when compared to NF treatment. Both T control and TS groups displayed luminescence intensity increased up to 250% with respect to their day 0, indicating a fast tumor growth rate and proving that NIR irradiation is necessary for this scaffold to show the anticancer effect. These results agree with our experimental findings on 4T1 in vitro. After two weeks, no luminescence signal was observed for both treatments, while both T and TS showed a further increase in tumor luminescence intensity, as a further proof of the anticancer effect of our photocancer therapy. The inhibition ratios of different NIR regimens were also calculated (Figure S1). These ratios showed that the PLGA-GO 2% scaffold under T3 NIR Irradiation regimen performed strongest inhibition to the tumor growth with a final ratio over 99% after 7 days treatment, confirming its high efficiency for tumor therapy.

3.11. Histological analysis

The tissue was examined histologically to evaluate the photothermal and photodynamic effect obtained by NIR irradiation (Fig. 11). Tumor histology in the T and TS groups exhibited high-grade carcinoma without significant lymphomonocytic infiltrate (Fig. 11A and B), wherein tissue analysis showed healthy skin without neoplasia in hematoxylin and eosin (H&E) stained images of NF and t3 groups (Fig. 11C and D). To determine whether PLGA or PLGA-GO 2% scaffold induce inflammatory response, at the end of the experiments, we evaluated the systemic release of key proinflammatory biomarkers. As shown in Figure S2, the serum levels of TNF-α and IL-6 were under the detection threshold in each group, indicating that the inflammatory response was not induced by in vivo exposure to scaffolds. MIP-2, a chemokine involved in the recruitment of acute inflammatory cells, was constitutively expressed at very low levels, showing no difference among the experimental groups. The body weight of all groups further revealed no significant difference, confirming that no obvious toxicity was induced by either PLGA or PLGA-GO 2% scaffolds (Figure S3). These results suggest that PLGA-GO 2% scaffold or + NIR irradiation significantly inhibited tumor growth and displayed excellent photothermal therapy ability in vivo.

3.12. In vivo photo dynamic therapy for non-direct contact tumors

To investigate the effect of NIR therapy on noncontact tumors, 4T1 cells were subcutaneously injected into tumor-bearing mice to establish a recurrent tumor model. In order to comprehensively assess the efficacy of our proposed fractionated photodynamic therapy, we conducted in vivo experiments utilizing a tumor site in proximity to the scaffold but not in direct contact with it. This deliberate choice aimed to simulate the clinical scenario of recurrent tumors that may reoccur in the same original treatment site but not in direct contact with the scaffold. One week after injection, scaffolds were implanted under the primary tumor and NIR radiation was performed. For this purpose, we focused on the therapeutic protocol that resulted in the highest antitumor efficiency, the fractionated dose t3. As for the previous experiment, we monitored the bioluminescence intensity after intraperitoneal injection of D-luciferin using the Optical Imaging IVIS® System, by acquiring images every 7 days (Fig. 12A). Results of % luminescence are shown in Fig. 12B. Both in direct contact (T I) and not in direct contact (T II) tumors depicted a significant growth of 272 ± 15 % and 215 ± 12 % respectively when compared to their day 0 in control group. Importantly, based on our evidence, both the treated in contact (t3 I) and the not in direct contact tumor (t3 II) of t3 showed a strongly significant reduction in tumor growth in terms of % luminescence. These findings furtherly verified the high antitumor effect of t3 NIR not only against primary tumor, but also against the not directly treated tumor, holding a great potential in the application of targeting cancer with no adverse effects.
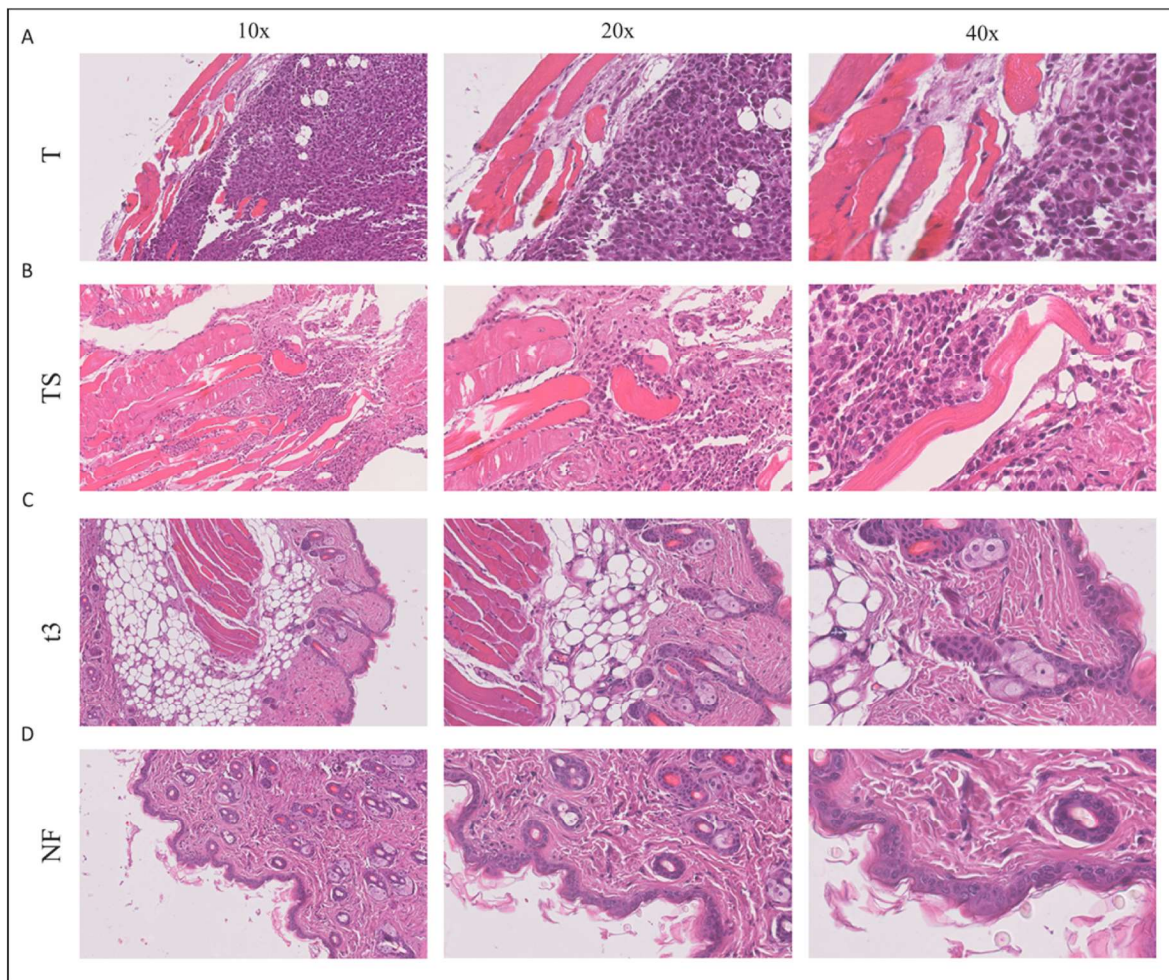
Fig. 11. Histological images of tissue samples from mice at 10×, 20× and 40× magnification. **A**) A Representative image of a T sample after the experimental timespan. **B**) Representative image of a TS sample after the experimental timespan. **C**) Representative image of a t3 sample after NIR radiation, showing healthy skin. **D**) Representative image of a NF sample after NIR radiation, showing healthy skin.

4. Conclusions

In this study, we report remarkable advancements in the field of biomaterials and tissue engineering, showcasing the use of 3D printing technology of PLGA-GO to create a potent therapeutic platform. The unique attributes of GO, including its biocompatibility, drug-loading capacity, and photothermal/photodynamic characteristics, position it as an ideal candidate for multifunctional therapeutics in cancer treatment. Importantly, this work marks the first attempt to optimize NIR radiation protocols for anticancer therapy. Our investigation focused on comparing two distinct photothermal/photodynamic therapeutic strategies – a single radiation session (NF) and a fractionated approach over three consecutive days (t1, t2, and t3) – utilizing innovative 3D printed GO-PLGA scaffolds. The comprehensive assessment encompassed both in vitro and in vivo evaluations, providing critical insights into the comparative efficacy of these strategies. Notably, in our in vitro experiments, we observed significant differences in response to the two different NIR doses. Cancer cells subjected to the single radiation session (NF) exhibited a shift in their death mechanisms towards necrosis. On the other hand, cancer cells treated with the fractionated dose (t3) displayed a different type of cell death, characterized by a shift towards apoptosis. In both in vitro and in vivo settings, the fractionated approach (t3) exhibited heightened efficacy in the eradication of cancer cells, thereby emphasizing its potential as a robust and precisely targeted strategy for anticancer intervention. Furthermore, our findings

highlighted the immense potential of NIR-mediated PTT/PDT in achieving targeted cancer cell eradication, enhancing immune polarization and stimulation The comprehensive evaluation of different doses of NIR radiation emphasizes the importance of optimizing and standardizing PTT/PDT protocols to maximize therapeutic benefits. This pioneering work adds to the mounting evidence supporting the clinical translation of NIR-based therapeutic approaches and underscores the need for further research to fully harness their potential in cancer therapy. In the context of surgical reconstruction after oncologic procedures, the incorporation of nanomaterials like graphene into scaffolds introduces an innovative dimension to cancer therapy. These scaffolds, tailored to specific anatomical sites, serve as strategic platforms for the localized delivery of PTT/PDT. Placing photosensitizing nanomaterials within these scaffolds enables targeted local treatments precisely where the risk of tumor recurrence is highest. This groundbreaking approach addresses a critical challenge in cancer therapy—the prevention of local recurrence following surgical interventions. By combining the precision of PTT/PDT with the unique properties of advanced nanomaterials, we open avenues for highly localized and effective treatments. In conclusion, our study not only emphasizes the effectiveness of 3D printed GO-PLGA scaffolds in cancer treatment but also unveils significant differences in response to the two distinct NIR doses both in vitro and in vivo. Our findings open avenues for the development of more potent and targeted therapies within the emerging field of PTT/PDT-based treatments.
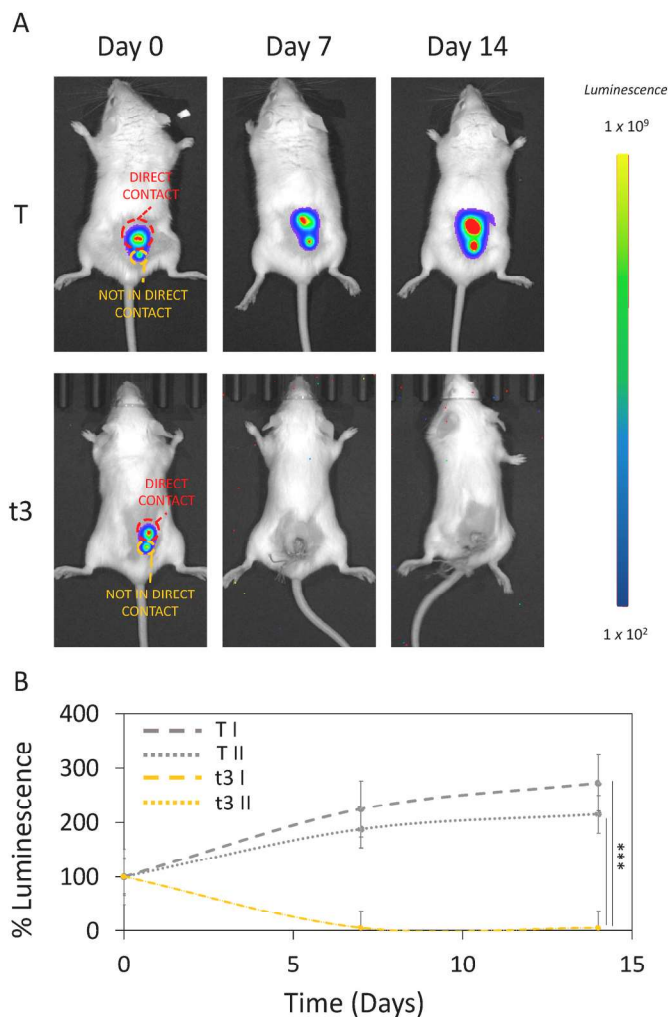
Fig. 12. In vivo NIR radiation against not in direct contact tumor. **A**) In vivo luminescence intensity on the two experimental groups, having an in direct contact and a not in direct contact tumor (T I, T II, t3 I and t3 II). **B**) Luminescence intensity over time. Luminescence was expressed as % of day 0 for each experimental group. ***$p < 0.001$ ANOVA and Turkey post-hoc test.

CRediT authorship contribution statement

Giordano Perini: Writing – original draft, Validation, Investigation, Formal analysis, Data curation. **Valentina Palmieri:** Visualization, Methodology, Investigation, Data curation. **Andrea Papait:** Writing – original draft, Formal analysis, Data curation. **Alberto Augello:** Methodology, Investigation, Formal analysis. **Daniela Fioretti:** Investigation, Formal analysis, Data curation. **Sandra Iurescia:** Investigation, Formal analysis, Data curation. **Monica Rinaldi:** Investigation, Formal analysis. **Elsa Vertua:** Formal analysis, Data curation. **Antonietta Silini:** Funding acquisition, Formal analysis. **Riccardo Torelli:** Methodology, Investigation, Formal analysis. **Angela Carlino:** Formal analysis, Data curation. **Teresa Musarra:** Formal analysis, Data curation. **Maurizio Sanguinetti:** Methodology, Investigation. **Ornella Parolini:** Methodology, Investigation, Formal analysis, Data curation. **Marco De Spirito:** Writing – review & editing, Validation, Methodology. **Massimiliano Papi:** Writing – review & editing, Supervision, Resources, Project administration, Methodology, Investigation, Funding acquisition, Data curation, Conceptualization.

Declaration of competing interest

The authors declare that they have no known competing financial interests or personal relationships that could have appeared to influence the work reported in this paper.

Appendix A. Supplementary data

Supplementary data to this article can be found online at https://doi.org/10.1016/j.mtbio.2024.100986.

References

[1] A.S. Sogomonyan, et al., 3D models of cellular spheroids as a universal tool for studying the cytotoxic properties of anticancer compounds in vitro, Acta Naturae 14 (2022) 92.
[2] J.O. Winter, S.S. Rao, Tissue Engineering Models for Cancer Pathology, 2022.
[3] A. Do, B. Khorsand, S.M. Geary, A.K. Salem, 3D printing of scaffolds for tissue regeneration applications, Adv. Healthcare Mater. 4 (2015) 1742–1762.
[4] F. Causa, P.A. Netti, L. Ambrosio, A multi-functional scaffold for tissue regeneration: the need to engineer a tissue analogue, Biomaterials 28 (2007) 5093–5099.
[5] G. Lutzweiler, A. Ndreu Halili, N. Engin Vrana, The overview of porous, bioactive scaffolds as instructive biomaterials for tissue regeneration and their clinical translation, Pharmaceutics 12 (2020) 602.
[6] N.Z. Laird, et al., Applications of nanotechnology in 3D printed tissue engineering scaffolds, Eur. J. Pharm. Biopharm. 161 (2021) 15–28.
[7] A. Zaszczyńska, B. Niemczyk-Soczynska, P. Sajkiewicz, A comprehensive review of electrospun fibers, 3D-printed scaffolds, and hydrogels for cancer therapies, Polymers 14 (2022) 5278.
[8] H. Bhuskute, P. Shende, B. Prabhakar, 3D printed personalized medicine for cancer: applications for betterment of diagnosis, prognosis and treatment, AAPS PharmSciTech 23 (2022) 1–12.
[9] V. Palmieri, et al., 3D-printed graphene for bone reconstruction, 2D Mater. 7 (2020) 22004.
[10] V. Palmieri, G. Perini, M. De Spirito, M. Papi, Graphene oxide touches blood:: in vivo interactions of bio-coronated 2D materials, Nanoscale Horiz. 4 (2019) 464–471.
[11] K. Krishnamoorthy, M. Veerapandian, K. Yun, S.J. Kim, The chemical and structural analysis of graphene oxide with different degrees of oxidation, Carbon N Y 53 (2013) 38–49.
[12] V. Palmieri, M. Papi, Can graphene take part in the fight against COVID-19? Nano Today (2020) 100883.
[13] A.G. Marrani, et al., A comparative experimental and theoretical study of the mechanism of graphene oxide mild reduction by ascorbic acid and N-acetyl cysteine for biomedical applications, Mater. Adv. 1 (2020) 2745–2754.
[14] F. De Maio, et al., 3D-printed graphene polylactic acid devices resistant to SARS-CoV-2: sunlight-mediated sterilization of additive manufactured objects, Carbon N Y 194 (2022) 34–41.
[15] G. Perini, V. Palmieri, G. Ciasca, M. De Spirito, M. Papi, Unravelling the potential of graphene quantum dots in biomedicine and neuroscience, Int. J. Mol. Sci. 21 (2020) 3712.
[16] V. Palmieri, et al., Graphene oxide-mediated copper reduction allows comparative evaluation of oxygenated reactive residues exposure on the materials surface in a simple one-step method, Appl. Surf. Sci. 615 (2023) 156315.
[17] T. Dutta, et al., ROS generation by reduced graphene oxide (rGO) induced by visible light showing antibacterial activity: comparison with graphene oxide (GO), RSC Adv. 5 (2015) 80192–80195.
[18] L. Jacquemin, et al., Mechanisms of radical formation on chemically modified graphene oxide under near infrared irradiation, Small 19 (2023) 2207229.
[19] Y. He, A. Del Valle, Y. Qian, Y.-F. Huang, Near infrared light-mediated enhancement of reactive oxygen species generation through electron transfer from graphene oxide to iron hydroxide/oxide, Nanoscale 9 (2017) 1559–1566.
[20] G. Perini, et al., Carboxylated graphene quantum dots-mediated photothermal therapy enhances drug-membrane permeability, ROS production, and the immune system recruitment on 3D glioblastoma models, Cancer Nanotechnol. 14 (2023) 13.
[21] F. Sun, et al., Application of 3D-printed, PLGA-based scaffolds in bone tissue engineering, Int. J. Mol. Sci. 23 (2022) 5831.

[22] L. Sutrisno, et al., PLGA–collagen–BPNS bifunctional composite mesh for photothermal therapy of melanoma and skin tissue engineering, J. Mater. Chem. B 10 (2022) 204–213.

[23] C.V. Rocha, V. Gonçalves, M.C. da Silva, M. Bañobre-López, J. Gallo, PLGA-based composites for various biomedical applications, Int. J. Mol. Sci. 23 (2022) 2034.

[24] L. Leung, C. Chan, S. Baek, H. Naguib, Comparison of morphology and mechanical properties of PLGA bioscaffolds, Biomed. Mater. 3 (2008) 025006.

[25] A.N.F. Versypt, D.W. Pack, R.D. Braatz, Mathematical modeling of drug delivery from autocatalytically degradable PLGA microspheres—a review, J. Contr. Release 165 (2013) 29–37.

[26] G. Perini, et al., Graphene quantum dots' surface chemistry modulates the sensitivity of glioblastoma cells to chemotherapeutics, Int. J. Mol. Sci. 21 (2020) 6301.

[27] G. Perini, et al., Inhibiting the growth of 3D brain cancer models with bio-coronated liposomal temozolomide, Pharmaceutics 13 (2021), https://doi.org/10.3390/pharmaceutics13030378. Preprint at.

[28] G. Perini, et al., Functionalized Graphene Quantum Dots Modulate Malignancy of Glioblastoma Multiforme by Downregulating Neurospheres Formation. *C*, vol. 7, 2021, https://doi.org/10.3390/c7010004. Preprint at.

[29] V. Palmieri, et al., Biocompatible: N -acetyl cysteine reduces graphene oxide and persists at the surface as a green radical scavenger, Chem. Commun. 55 (2019) 4186–4189.

[30] G. Perini, et al., Advanced usage of Ti3C2Tx MXenes for photothermal therapy on different 3D breast cancer models, Biomed. Pharmacother. 153 (2022) 113496.

[31] A. Rosenkranz, et al., Laser-mediated antibacterial effects of few- and multi-layer Ti3C2Tx MXenes, Appl. Surf. Sci. 567 (2021) 150795.

[32] M.B. Ericson, A.-M. Wennberg, O. Larkö, Review of photodynamic therapy in actinic keratosis and basal cell carcinoma, Therapeut. Clin. Risk Manag. 4 (2008) 1–9.

[33] J. Usuda, et al., Photodynamic therapy (PDT) for lung cancers, J. Thorac. Oncol. 1 (2006) 489–493.

[34] T. Kubrak, M. Karakuła, M. Czop, A. Kawczyk-Krupka, D. Aebisher, Advances in management of bladder cancer—the role of photodynamic therapy, Molecules 27 (2022).

[35] P. Sekhri, D.K. Ledezma, A. Shukla, E.E. Sweeney, R. Fernandes, The thermal dose of photothermal therapy generates differential immunogenicity in human neuroblastoma cells, Cancers 14 (2022) 1447.

[36] M. Overchuk, R.A. Weersink, B.C. Wilson, G. Zheng, Photodynamic and photothermal therapies: synergy opportunities for nanomedicine, ACS Nano 17 (2023) 7979–8003.

[37] A.R. Silini, et al., CM from intact hAM: an easily obtained product with relevant implications for translation in regenerative medicine, Stem Cell Res. Ther. 12 (2021) 540.

[38] T. Arasoglu, S. Derman, B. Mansuroglu, Comparative evaluation of antibacterial activity of caffeic acid phenethyl ester and PLGA nanoparticle formulation by different methods, Nanotechnology 27 (2016) 25103.

[39] D. Edith, J.-L. Six, Surface characteristics of PLA and PLGA films, Appl. Surf. Sci. 253 (2006) 2758–2764.

[40] S. Chaiyakun, et al., Preparation and characterization of graphene oxide nanosheets, Procedia Eng. 32 (2012) 759–764.

[41] A.G. Marrani, R. Zanoni, R. Schrebler, E.A. Dalchiele, Toward graphene/silicon interface via controlled electrochemical reduction of graphene oxide, J. Phys. Chem. C 121 (2017) 5675–5683.

[42] C.-H. Lee, C.-H. Hong, W.-T. Liao, H.-S. Yu, Differential immunological effects of infrared irradiation and its associated heat in vivo, J. Photochem. Photobiol., B 155 (2016) 98–103.

[43] W.-T. Liao, et al., Anti-Inflammatory effects induced by near-infrared light irradiation through M2 macrophage polarization, J. Invest. Dermatol. 141 (2021) 2056–2066.

[44] P. Xu, F. Liang, Nanomaterial-based tumor photothermal immunotherapy, Int. J. Nanomed. 15 (2020) 9159.

[45] C. Xu, Y. Jiang, Y. Han, K. Pu, R. Zhang, A polymer multicellular nanoengager for synergistic NIR-II photothermal immunotherapy, Adv. Mater. 33 (2021) 2008061.

[46] R.L. Randall, A promise to our patients with metastatic bone disease, Ann. Surg Oncol. 21 (2014) 4049–4050.

[47] G. Gravis, Systemic treatment for metastatic prostate cancer, Asian J. Urol. 6 (2019) 162–168.

[48] J.W. Hartley, et al., Expression of infectious murine leukemia viruses by RAW264. 7 cells, a potential complication for studies with a widely used mouse macrophage cell line, Retrovirology 5 (2008) 1–6.

[49] L.E. DeForge, D.G. Remick, Kinetics of TNF, IL-6, and IL-8 gene expression in LPS-stimulated human whole blood, Biochem. Biophys. Res. Commun. 174 (1991) 18–24.

[50] M. Pérez-Hernández, et al., Dissecting the molecular mechanism of apoptosis during photothermal therapy using gold nanoprisms, ACS Nano 9 (2015) 52–61.

[51] Y. Zhang, et al., Temperature-dependent cell death patterns induced by functionalized gold nanoparticle photothermal therapy in melanoma cells, Sci. Rep. 8 (2018) 8720.

[52] M. Kim, et al., Numerical study on effective conditions for the induction of apoptotic temperatures for various tumor aspect ratios using a single continuous-wave laser in photothermal therapy using gold nanorods, Cancers 11 (2019), https://doi.org/10.3390/cancers11060764. Preprint at.

[53] C.J.F. Van Noorden, The history of Z-VAD-FMK, a tool for understanding the significance of caspase inhibition, Acta Histochem. 103 (2001) 241–251. Preprint at.

[54] S.H. Needs, M.D. Bootman, J.E. Grotzke, H.B. Kramer, S.A. Allman, Off-target inhibition of NGLY1 by the polycaspase inhibitor Z-VAD-fmk induces cellular autophagy, FEBS J. 289 (2022) 3115–3131.

[55] H. Ushijima, R. Monzaki, An in vitro evaluation of the antioxidant activities of necroptosis and apoptosis inhibitors: the potential of necrostatin-1 and necrostatin-1i to have radical scavenging activities, Pharmacol. Rep. 75 (2023) 490–497.